



## Thermoelastic stresses alleviation for two-dimensional functionally graded cylinders under asymmetric loading

A. M. Eldeeb, Y. M. Shabana, T. A. El-Sayed, Licheng Guo & A. Elswaf

To cite this article: A. M. Eldeeb, Y. M. Shabana, T. A. El-Sayed, Licheng Guo & A. Elswaf (2023) Thermoelastic stresses alleviation for two-dimensional functionally graded cylinders under asymmetric loading, Journal of Thermal Stresses, 46:1, 59-74, DOI: [10.1080/01495739.2022.2151960](https://doi.org/10.1080/01495739.2022.2151960)

To link to this article: <https://doi.org/10.1080/01495739.2022.2151960>



© 2022 The Author(s). Published with license by Taylor & Francis Group, LLC.



Published online: 06 Dec 2022.



Submit your article to this journal [↗](#)



Article views: 316








View related articles [↗](#)



View Crossmark data [↗](#)

# Thermoelastic stresses alleviation for two-dimensional functionally graded cylinders under asymmetric loading

A. M. Eldeeb<sup>a,b,c</sup> , Y. M. Shabana<sup>a</sup> , T. A. El-Sayed<sup>a,d</sup> , Licheng Guo<sup>b</sup> , and A. Elsawaf<sup>e</sup> 

<sup>a</sup>Mechanical Design Department, Faculty of Engineering, El-Mataria, Helwan University, Cairo, Egypt;

<sup>b</sup>Department of Astronautic Science and Mechanics, Harbin Institute of Technology, Harbin, China;

<sup>c</sup>Department of Mechanical Engineering, Lyle School of Engineering, Southern Methodist University, Dallas, TX, USA;

<sup>d</sup>Centre for Applied Dynamics Research, School of Engineering, University of Aberdeen, Aberdeen, United Kingdom;

<sup>e</sup>Mechanical Engineering Department, College of Engineering and Technology-Cairo

Campus, Arab Academy for Science, Technology and Maritime Transport (AASTMT), Cairo, Egypt

## ABSTRACT

The goal of this research study is to examine, through the finite element method, the efficiency of using two-dimensional (2D) functionally graded materials (FGMs) in lowering the elastic/thermoelastic stresses acting on cylinders. In 2D-FGMs, the properties are assumed to vary in the radial and tangential directions simultaneously, which is rarely investigated in the literature. The cylinder is subjected to asymmetric inner normal traction with/without asymmetric thermal loading. For the considered case studies, results revealed that 2D-FGMs is beneficial compared to the conventional grading. In case of considering mechanical load only, the tangential stress declines by almost 39%. Similarly, accounting for thermomechanical load resulted in radical falls for the tangential and axial stresses by around 63% and 61%, respectively. Accordingly, the von Mises stress declines dramatically with different values allowing for safe load escalation, and enhancing the cylinder's durability. Finally, no certain values for the used tangential function's parameters are preferred to have maximum reduction of stresses under all working circumstances, which necessitates performing optimization.

## ARTICLE HISTORY

Received 19 July 2022

Accepted 7 November 2022



## KEYWORDS

Asymmetric loading; finite element method; functionally graded materials; stationary cylinder; thermoelastic analysis; von Mises stress

## 1. Introduction

Functionally graded materials (FGMs) are extensively used in many engineering applications due to their sophisticated properties. Many authors investigated the behaviors of different functionally graded (FG) structures, such as plates, cylinders, and discs. For plates, Cong et al. [1], for example, showed that the porosity had significant impacts on the thermomechanical buckling and post-buckling of FG cylinder (FGCs). Kouider et al. [2] examined the effects of the volume fraction, geometrical parameters, and heterogeneity index on the bending and free vibration responses of FG sandwich plates. Others were concerned with the fracture of such structures (e.g., see Refs. [3, 4]).

Regarding FGCs, many parameters were investigated under different load types (mechanical, thermal, electrical, magnetic, etc.) and conditions (symmetric, asymmetric), see for instance Refs. [5–7]. For example, Tokovyy and Ma [8] examined the performance of heterogeneous 1D-FGCs (1D: one-dimensional) subjected to partial thermal/mechanical loading with material properties radially graded. In

**CONTACT** T. A. El-Sayed  [tamer.el-sayed@abdn.ac.uk](mailto:tamer.el-sayed@abdn.ac.uk)  Mechanical Design Department, Faculty of Engineering, El-Mataria, Helwan University, P.O. Box 11718, Cairo, Egypt.

© 2022 The Author(s). Published with license by Taylor & Francis Group, LLC.

This is an Open Access article distributed under the terms of the Creative Commons Attribution License (<http://creativecommons.org/licenses/by/4.0/>), which permits unrestricted use, distribution, and reproduction in any medium, provided the original work is properly cited.

addition, Batra and Nie [9] used the polar form of the Fourier expansion and the method of Frobenius series to solve the differential equations of eccentric hollow FGCs. An exponential grading model was used by Loghman et al. [10], as well, while scrutinizing the performance of FGCs subjected to nonsymmetrical magneto-thermomechanical loads. Furthermore, the decelerating behaviors of multilayer 1D-FGCs under thermoelastic loads were explored while considering the materials' properties temperature dependency [11]. Analogous analyses could be found studying the behaviors of 1D-FG discs [12–15].

On a related front, researchers and industry seek lowering the stresses that encounter any mechanical structure to raise its lifetime, durability, safety level, and loading capacity. This also reduces the failure probability. Such goals could be achieved through different means that include but not limited to: optimization of some parameters 16–18, modifying the microstructure to yield a new material with desired properties [19] that includes higher strength [20], or developing two-dimensional (2D: two-dimensional) FGMs [21, 22]. This article is concerned with the later method, where a property becomes dependent on two directions. This method is rarely examined in contrast to the large number of articles discussing 1D-FG structures. For 2D-FGMs, to name just a few, Nemat-Alla [23] showed that they yielded improved performance than 1D-FGMs. Researches on 2D-FGMs are easily found in the Cartesian coordinates, see for instance Refs. [21, 24, 25]. However, in polar coordinates, limited numbers considered it as a combination between both the radial and axial directions [22, 26–30]. On the contrary, extremely rare articles were devoted to considering the variation with respect to the radial and tangential directions, see for example Ref. [31, 32].

In view of the aforementioned comprehensive literature review, the goal of this article is to examine the effectiveness of using 2D-FGMs in alleviating the stresses encountering FGCs, compared to the traditional 1D-FGCs. The properties would vary in both the radial and tangential directions simultaneously. In addition, a finite element (FE) scheme is built to solve the differential equations. Two examples are presented: one with mechanical load only, and the other includes a thermomechanical load. For each example, the idea of applying 2D-FGMs is presented, and its associated results are discussed.

## 2. Problem formulation

Using polar coordinates  $(r, \theta, z)$ , a stationary cylinder with inner and outer radii  $r_i$  and  $r_o$ , respectively, is considered. The mechanical equilibrium equations in the radial and tangential directions are written as [33]:

$$(r\sigma_r)_{,r} + \tau_{r\theta,\theta} - \sigma_\theta = 0 \quad (1)$$

$$(r\tau_{r\theta})_{,r} + \sigma_{\theta,\theta} + \tau_{r\theta} = 0 \quad (2)$$

where a comma denotes partial differentiation.  $\sigma_r$ ,  $\sigma_\theta$ ,  $\sigma_z$ , and  $\tau_{r\theta}$  ( $\varepsilon_r$ ,  $\varepsilon_\theta$ ,  $\varepsilon_z$ , and  $\varepsilon_{r\theta}$ ) are the radial, circumferential, axial, and shear stresses (strains), respectively, which are evaluated via the constitutive equations (Hooke's law) as follows [34]:

$$\boldsymbol{\sigma} = \mathbf{C}[\boldsymbol{\varepsilon} - \boldsymbol{\alpha}\mathbf{T}] \quad (3)$$

with

$$\boldsymbol{\sigma} = \begin{Bmatrix} \sigma_r \\ \sigma_\theta \\ \sigma_z \\ \tau_{r\theta} \end{Bmatrix}, \quad \boldsymbol{\varepsilon} = \begin{Bmatrix} \varepsilon_r = u_{,r} \\ \varepsilon_\theta = (u + \vartheta_{,\theta})/r \\ \varepsilon_z = w_{,z} \\ 2\varepsilon_{r\theta} = \vartheta_{,r} + (u_{,\theta} - \vartheta)/r \end{Bmatrix} \quad (4)$$

$$\mathbf{C} = \begin{bmatrix} C_{11} & C_{12} & C_{12} & 0 \\ & C_{11} & C_{12} & 0 \\ & & C_{11} & 0 \\ \text{sym} & & & C_{66} \end{bmatrix}, \quad \boldsymbol{\alpha} = \alpha \begin{Bmatrix} 1 \\ 1 \\ 1 \\ 0 \end{Bmatrix} \quad (5)$$

where  $\alpha$  is the thermal expansion coefficient,  $T$  is the temperature field (considering  $0^\circ\text{C}$  as a reference temperature),  $u$ ,  $\vartheta$ , and  $w$  are the radial, tangential, and axial displacements, respectively. For consistency, it should be noted that the natural shearing strain ( $\varepsilon_{r\theta}$ ) is the one used here, and it is equal to half of the engineering shear strain. Besides, for an isotropic material, Eq. (6) lists the materials' stiffness constants ( $C_{11}$ ,  $C_{12}$  and  $C_{66} = (C_{11} - C_{12})/2$ ) that are dependent on  $E$  (elastic constant) and  $\nu$  (Poisson's ratio).

$$\left\{ \begin{array}{l} C_{11} = \frac{E}{1 - \nu^2}, \quad C_{12} = \frac{E\nu}{1 - \nu^2} \rightarrow \text{Plane stress} \\ C_{11} = \frac{E(1 - \nu)}{(1 + \nu)(1 - 2\nu)}, \quad C_{12} = \frac{E\nu}{(1 + \nu)(1 - 2\nu)} \rightarrow \text{Plane strain} \end{array} \right. \quad (6)$$

In terms of  $T$ , it is dependent on the thermal conductivity ( $k$ ), and is obtained through solving the steady-state heat conduction equation in the 2D polar coordinates [31]:

$$\frac{1}{r}(rkT_{,r})_{,r} + \frac{1}{r^2}(kT_{,\theta})_{,\theta} = 0 \quad (7)$$

### 3. Finite element formulation

The finite element method (FEM) is widely used in modeling the behaviors of complicated problems in structural mechanics since it is known for its powerfulness and robustness. So, a FE scheme is developed through Matlab software to obtain  $u$ ,  $\vartheta$ , and  $T$ . The domain is discretized using the eight-node ( $n_n = 8$ ) isoparametric 2D elements with three degrees of freedom ( $u$ ,  $\vartheta$ , and  $T$ ) at each node. In FEM,  $u$ ,  $\vartheta$ , and  $T$  are approximately related to the corresponding nodal values through introducing number of shape functions  $N$  [35]:

$$u \approx \sum_{i=1}^{n_n} N_i^e u_i, \quad \vartheta \approx \sum_{i=1}^{n_n} N_i^e \vartheta_i, \quad T \approx \sum_{i=1}^{n_n} N_i^e T_i \quad (8)$$

where  $N_i^e$  is the element  $e$  shape function at the  $i$ th node.

Afterward, the standard Galerkin's procedures are followed to obtain the following symbolic FE equation [35]:  $\mathbf{Kd} = \mathbf{R}$ , where  $\mathbf{K}$  represents the global stiffness matrix,  $\mathbf{d} = \{\mathbf{U} \ \mathbf{T}\}$ ,  $\mathbf{U}$  includes both of  $u$  and  $\vartheta$ , and  $\mathbf{R}$  is the external force vector. In more detail, the FE discretized equation for a system composed of total number of elements  $n_e$  is:

$$\sum_{e=1}^{n_e} \left( \begin{bmatrix} \mathbf{K}_{UU}^e & \mathbf{K}_{UT}^e \\ \mathbf{K}_{TU}^e & \mathbf{K}_{TT}^e \end{bmatrix} \begin{Bmatrix} \mathbf{U}^e \\ \mathbf{T}^e \end{Bmatrix} = \begin{Bmatrix} \mathbf{R}_U^e \\ \mathbf{R}_T^e \end{Bmatrix} \right) \quad (9)$$

with  $\mathbf{K}^e$  and  $\mathbf{R}^e$  are the  $e$ th element stiffness matrix and force vector, respectively. They are determined as follows:

$$\begin{aligned} \mathbf{K}_{UU}^e &= \int_{\Omega_e} r[\mathbf{B}_U][\mathbf{C}][\mathbf{B}_U]d\Omega_e & \mathbf{K}_{UT}^e &= - \int_{\Omega_e} r[\mathbf{B}_U][\lambda][\mathbf{N}]d\Omega_e \\ \mathbf{K}_{TU}^e &= 0 & \mathbf{K}_{TT}^e &= \int_{\Omega_e} r[\mathbf{B}_T][\mathbf{k}][\mathbf{B}_T]d\Omega_e \\ \mathbf{R}_U^e &= \int_{\Gamma} r[\mathbf{N}]\sigma_n d\Gamma & \mathbf{R}_T^e &= 0 \end{aligned} \quad (10)$$

where  $\Omega_e$  is the element's domain such that  $d\Omega_e = r dr d\theta$ ,  $\Gamma$  is part of the boundary with specified tractions  $\sigma_n$ ,  $\lambda = \mathbf{C}\alpha$ , and  $\mathbf{k}$  is the thermal conductivity matrix. Also,  $\mathbf{B}_U$  is the strain-displacement matrix, and  $\mathbf{B}_T$  is the gradient matrix [36]. These integrations are executed using the gauss quadrature method with  $3 \times 3$  integration points within the element.

At this stage, the vector  $\mathbf{d}$  can easily be obtained ( $\mathbf{d} = \mathbf{K}^{-1}\mathbf{R}$ ). Then, strains and stresses are calculated directly through the standard steps of FEM at the gauss points within the element after applying the proper boundary conditions, and then extrapolated to the nodes, where they are averaged based on a node's location [36].

#### 4. Results and discussion

In this study, the results published by Li and Liu [37] are regenerated to benchmark the accuracy of the developed FE Matlab code. In Ref. [37], a stationary cylinder with  $r_o = 3r_i$  under plane strain conditions ( $\varepsilon_z = 0$ ) was investigated. The power-law model was selected to describe the gradation of some properties [37]:

$$\beta(r) = \beta_i + (\beta_o - \beta_i) \left( \frac{r - r_i}{r_o - r_i} \right)^\eta \quad (11)$$

where  $\beta$  is a generic material property, and  $\eta$  is the heterogeneity index that the impacts of its variation were extensively examined in prior studies (e.g., see Refs. [38–41]). Also, the two subscripts  $i$  and  $o$  refer to the property at  $r_i$  and  $r_o$ , respectively. Li and Liu [37] only proposed that  $E$  was varying according to Eq. (11), with  $E_i = 200$  GPa and  $E_o = E_i/3$  (Figure 1 shows its distribution), while  $\eta = 1$ , and  $\nu$  was kept constant at 0.28.

For loading, the inner circumference was subjected to a sinusoidal normal traction:  $\sigma_r(r_i, \theta) = p_0 \cos(n_p \theta)$ , where  $p_0 = 100$  MPa is the pressure amplitude, and  $n_p = 2$  is the normal traction coefficient. Whereas, the cylinder's outer edge was kept free of stress.

Regarding FEM, different number of elements along the radial and tangential directions was tested. After checking the mesh dependency, a great agreement is found to occur at  $n_e = 20,000$  (100 and 200 elements in  $r$  and  $\theta$  directions, respectively), as depicted in Figure 2 where dimensionless (normalized) stresses are plotted. It should be noted that, henceforth, any stress component is divided by  $p_0$  to be normalized.

Then, using the same example, the idea of applying the principle of 2D-FGMs is examined to mitigate the stresses through the cylinder. In other words,  $\beta$  would be a function in both  $r$  and  $\theta$ . This idea has been rarely investigated in the literature as shown previously in Section 2. Mathematically, this is to be accomplished by implementing a known function  $f(\theta)$  into Eq. (11). Such function can take any formula, for instance, exponential [31], trigonometric/polynomial [32], etc. Here, the focus would be directed toward the trigonometric function: cosine, such that:

$$f(\theta) = \cos(n_\theta \theta + s) \quad (12)$$

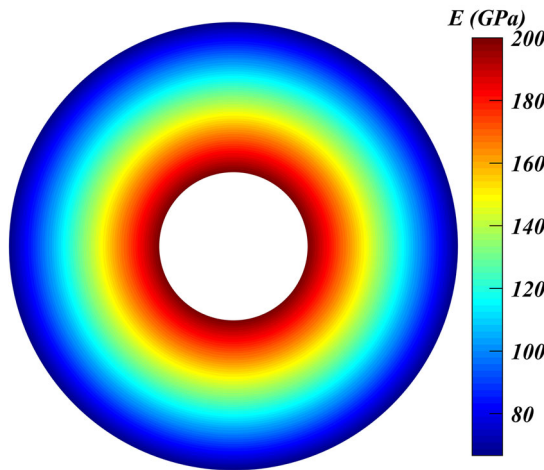
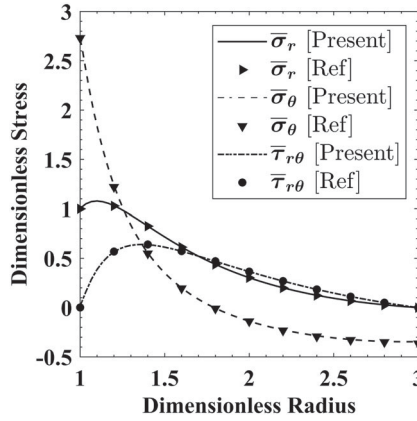


Figure 1. Contour plot for the distribution of  $E$  using Eq. (11).



**Figure 2.** Dimensionless stresses distribution from the current study and Ref. [37].  $\bar{\sigma}_r$  and  $\bar{\sigma}_\theta$  are plotted at  $\theta = 0^\circ$ , and  $\bar{\tau}_{r\theta}$  is plotted at  $\theta = +45^\circ$ .

where the angular (frequency) coefficient  $n_\theta = 1$  or  $2$  [32], and  $s$  is the shifting (phase) angle that is to be investigated, and its selected values  $\in [-180, 180]$ . Therefore, Eq. (11) becomes as follows after being multiplied by  $f(\theta)$  [Eq. (12)]:

$$\check{\beta}(r, \theta) = f(\theta) \times \left( \beta_i + (\beta_o - \beta_i) \left( \frac{r - r_i}{r_o - r_i} \right)^\eta \right) \tag{13}$$

where  $\check{\beta}$  is the modified property in the  $r$  and  $\theta$  directions. However, the nature of the cosine function would yield negative values of any property and escalates the positive value; hence, comparing results would not be reasonable. Thus, the following modification is proposed to keep  $\check{\beta}$  within the limits ( $\beta_i$  and  $\beta_o$ ):

$$\beta(r, \theta) = \beta_i + \left( \frac{\check{\beta}(r, \theta) - \min(\check{\beta})}{\max(\check{\beta}) - \min(\check{\beta})} \right) (\beta_o - \beta_i) \tag{14}$$

To make sure that there is no confusion occurs for the reader, Figure 3 presents, for instance, the variation of  $E$  at  $n_\theta = 2$  and  $1$  with different values of  $s$ , where the harmonic pattern of the cosine function appears clearly.

At the beginning, the impacts of  $n_\theta = 2$ , while  $s$  taking either the values of  $0^\circ$ ,  $-30^\circ$ ,  $-90^\circ$ , and  $180^\circ$ , are studied. Using Eq. (11) produces the contours depicted in Figure 4 with  $\bar{\sigma}_{r\max} = -\bar{\sigma}_{r\min} = 1.1$ ,  $\bar{\sigma}_{\theta\max} = -\bar{\sigma}_{\theta\min} = 2.75$  and  $\bar{\tau}_{r\theta\max} = -\bar{\tau}_{r\theta\min} = 0.67$ . It should be mentioned that, henceforth, subscripts max and min are used to refer to a quantity's upper and lower values, respectively.

Enhanced results are obtained upon applying Eq. (14). The stresses' contours for the selected values of  $s$  are presented in Figures 5–8. Evidently, the three stress components experienced different rates of reduction. However,  $\bar{\sigma}_\theta$  is the component that witnessed the significant drop compared to  $\bar{\sigma}_r$  and  $\bar{\tau}_{r\theta}$ .

For  $\bar{\sigma}_{r\max}$ , nearly 7.7% reduction is applicable at  $s = 0$  (Figure 5a). This percentage declines if another value of  $s$  is chosen. However, at such instant ( $s \neq 0$ ),  $\bar{\sigma}_{r\min}$  showed an increase in the decline percentage hitting 7.6% at  $s = 180^\circ$  as depicted in Figure 8a. Regarding  $\bar{\tau}_{r\theta}$ , its upper and lower values almost remained static around a value of  $\pm 0.55$  which resembles a moderate decline. For example, in Figure 6c, both of them declined by nearly 17.3% at  $s = 0$ . This percentage approached 20% at  $s = -90^\circ$  for  $\bar{\tau}_{r\theta\min}$  as shown in Figure 7c.

Then, when it comes to  $\bar{\sigma}_\theta$ , it can be stated that 2D-FGMs are absolutely advantageous. Numbers reveal that at  $s = 0^\circ$  (Figure 5b),  $\bar{\sigma}_{\theta\max}$  went down steeply by  $\sim 39\%$  compared to the

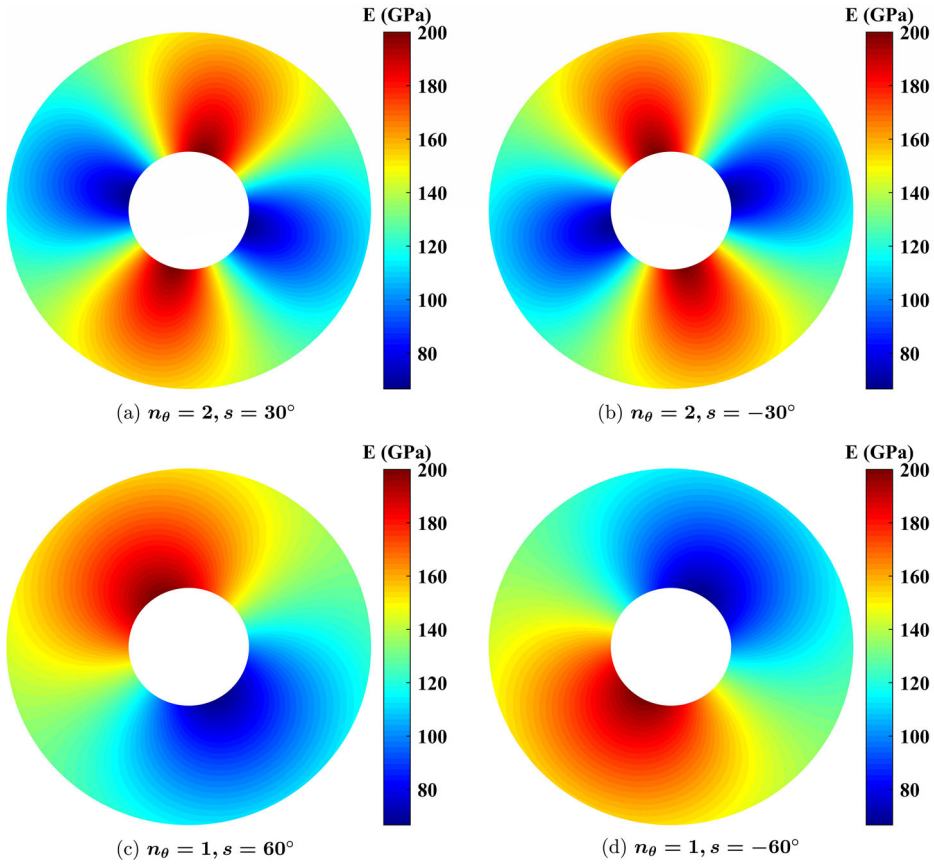


**Figure 3.** Contour plots for  $E$  using Eq. (14).

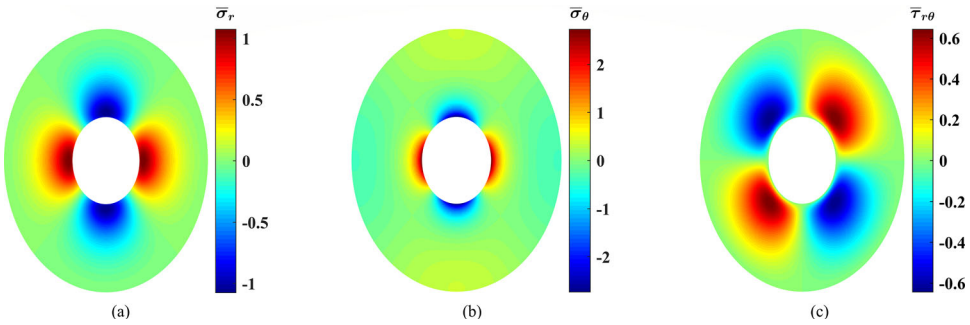


**Figure 4.** Dimensionless stress contours based on FEM solution for 1D-FGC. (a) Dimensionless radial stress, (b) dimensionless tangential stress, and (c) dimensionless shear stress.

value of 1D-FGMs. Conversely, according to Figure 8b it declined moderately by  $\sim 10\%$  at  $s = 180^\circ$ . Similarly, at  $s = -30^\circ$ , it is depicted in Figure 6b that  $\bar{\sigma}_{\theta_{\max}}$  and  $\bar{\sigma}_{\theta_{\min}}$  declined significantly by approximately 38% and 12.5%, respectively.

Furthermore, Figure 9 presents the reduction values occurring in the extreme values of each stress component at  $n_\theta = 2$  and  $n_\theta = 1$  at different values of  $s$ . Generally, it is found that there are no differences obtained when the sign of  $s$  changes as  $f(\theta)$  has a similar harmonic pattern to the only present load. Also, in this case of loading, the use of  $n_\theta = 2$  (Figure 9a) produced larger reductions than  $n_\theta = 1$  (Figure 9b).

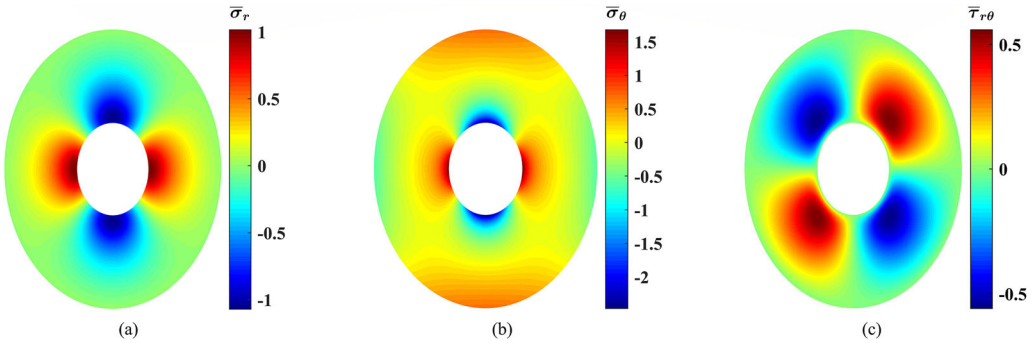


**Figure 5.** Dimensionless stress contours for  $f(\theta) = \cos(2\theta + 0^\circ)$ . (a) Dimensionless radial stress, (b) dimensionless tangential stress, and (c) dimensionless shear stress.

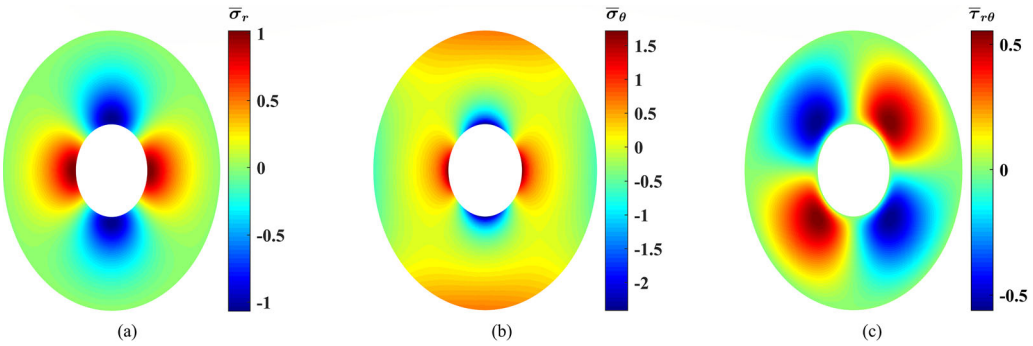


**Figure 6.** Dimensionless stress contours for  $f(\theta) = \cos(2\theta - 30^\circ)$ . (a) Dimensionless radial stress, (b) dimensionless tangential stress, and (c) dimensionless shear stress.

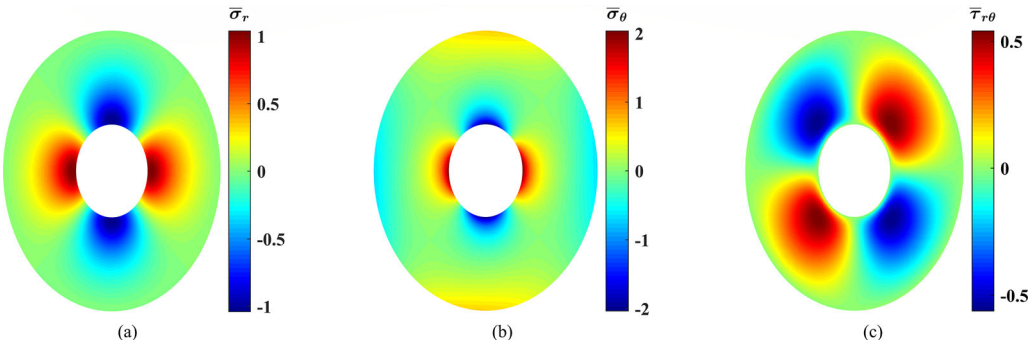


**Figure 7.** Dimensionless stress contours for  $f(\theta) = \cos(2\theta - 90^\circ)$ . (a) Dimensionless radial stress, (b) dimensionless tangential stress, and (c) dimensionless shear stress.

It can be stated that all the stress values witnessed different percentages of reduction. Since  $\sigma_\theta$  has higher value compared to  $\sigma_r$  and  $\tau_{r\theta}$ , the focus would be directed toward it. If a designer chooses  $s = 0$  (Figure 9a), a reduction of nearly 39% and 10% is applicable for  $\bar{\sigma}_{\theta_{\max}}$  and  $\bar{\sigma}_{\theta_{\min}}$ , respectively. Since,  $|\bar{\sigma}_{\theta_{\min}}| > |\bar{\sigma}_{\theta_{\max}}|$ ; therefore,  $\bar{\sigma}_{\theta_{\min}}$  is the cylinder's load limit decisive parameter if considered individually. However, the small reduction in  $\bar{\sigma}_{\theta_{\max}}$  is critical in most composites since metals have limited tensile strength compared to the huge compressive strength of ceramics that necessitates higher reduction in  $\bar{\sigma}_{\theta_{\max}}$ . In contrast, Figure 9a depicts that a compromise ( $\sim 26\%$  reduction) is applicable between the two percentages at  $s = \pm 90^\circ$ , which is



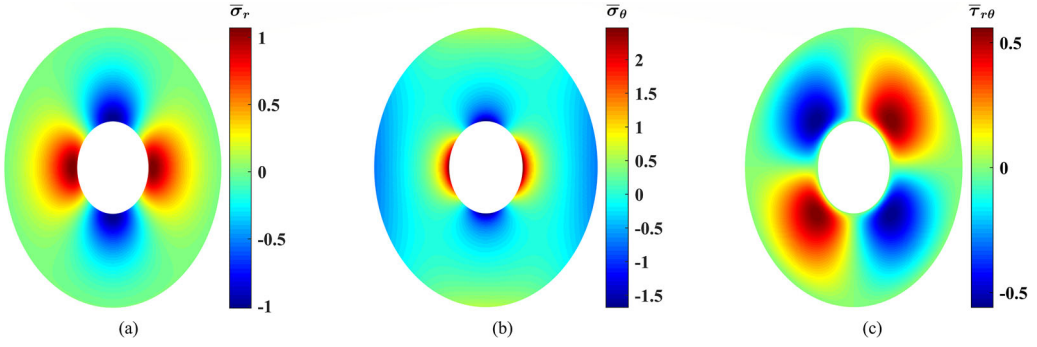


**Figure 8.** Dimensionless stress contours for  $f(\theta) = \cos(2\theta + 180^\circ)$ . (a) Dimensionless radial stress, (b) dimensionless tangential stress, and (c) dimensionless shear stress.

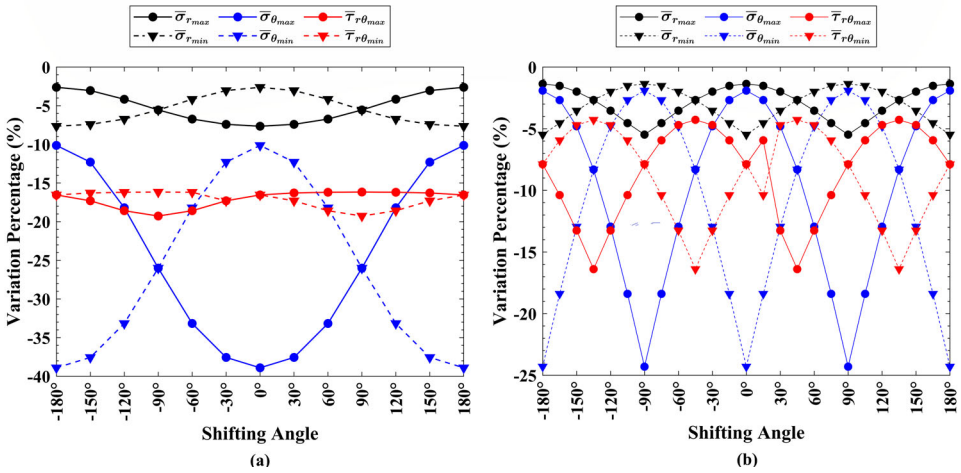


**Figure 9.** Percentages of stresses reduction at different values of  $s$  for  $f(\theta) = \cos(n_\theta\theta + s)$ : (a)  $n_\theta = 2$ , and (b)  $n_\theta = 1$ .

similar to predictions concluded from Figure 9b at  $s = \pm 45^\circ$  and  $\pm 135^\circ$  where a decline by almost 9% is attainable. Such points can be considered as the optimum points.

Based on the aforementioned results, it can be stated that using 2D-FGMs would significantly mitigate stresses allowing for load escalation. To make sure that this advantage always happens, the second example is presented, where thermomechanical loading is present. The following material properties are considered in addition to the previously mentioned ones with  $\eta = 1$ :  $k_i = 209\text{W/mK}$ ,  $k_o = 2\text{W/mK}$ ,  $\alpha_i = 23 \times 10^{-6}/^\circ\text{C}$ , and  $\alpha_o = 10^{-5}/^\circ\text{C}$  [42]. In addition, the following boundary conditions are used:

$$\begin{cases} \sigma_r(r_i, \theta) = p_0 \cos(n_p \theta) Pa, & \tau_{r\theta}(r_i, \theta) = 0 \\ T(r_i, \theta) = T_0 + 50 \sin(n_T \theta) ^\circ\text{C} \\ u_r(r_o, \theta) = u_\theta(r_o, \theta) = 0 \\ T(r_o, \theta) = 0^\circ\text{C} \end{cases} \quad (15)$$

where  $T_0$  is the reference temperature, and  $n_T$  is the temperature's coefficient.

Figure 10 presents the resulting temperature profile and stresses, for the 1D-FGC at  $n_p = n_T = 2$ ,  $T_0 = 100^\circ\text{C}$ , and  $p_0 = 100\text{MPa}$ . At this stage, another comparing parameter is introduced: the von Mises stress ( $\sigma_{VM}$ ) that is calculated according to Eq. (16) [43]. In the dimensionless form, it becomes:  $\bar{\sigma}_{VM} = \sigma_{VM}/p_0$ .

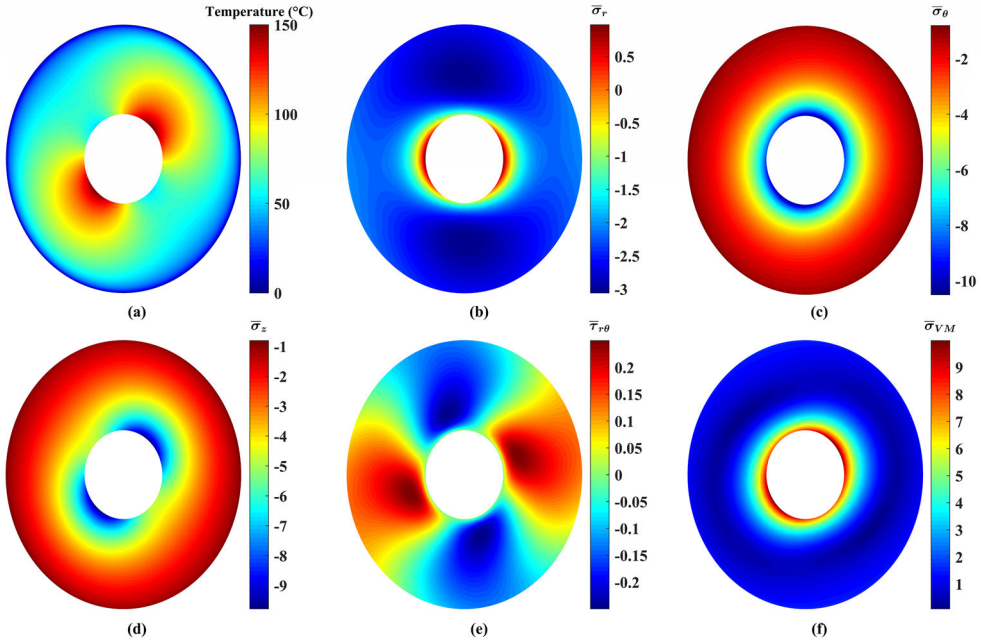


**Figure 10.** Resulting contours of the thermoelastic problem of 1D-FGC ( $f(\theta) = 1$ ). (a) Temperature, (b) dimensionless radial stress, (c) dimensionless tangential stress, (d) dimensionless axial stress, (e) dimensionless shear stress, and (f) dimensionless von Mises stress.

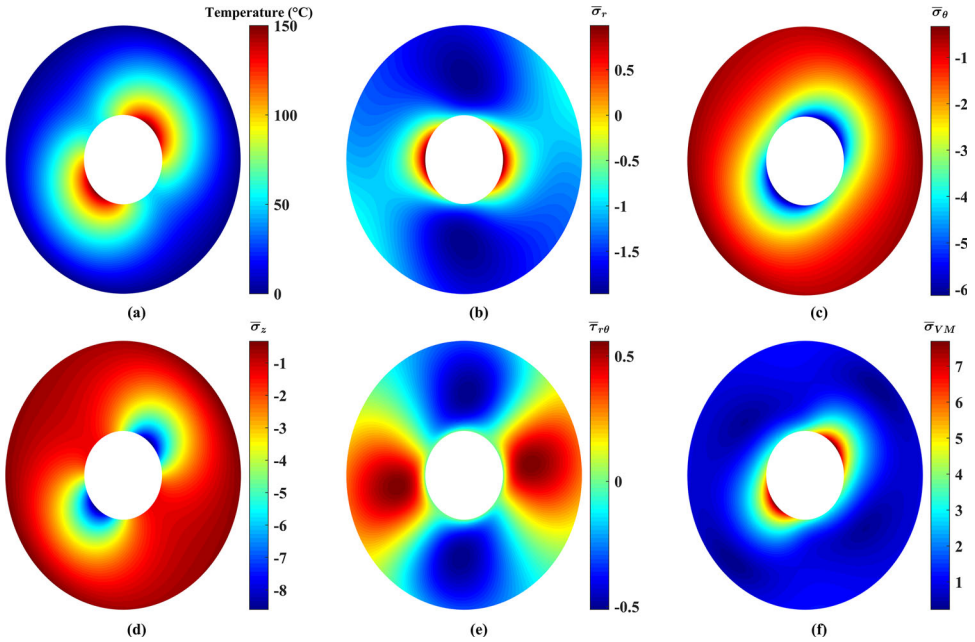


**Figure 11.** Resulting contours of the thermoelastic problem of 2D-FGC with  $f(\theta) = \cos(2\theta + 90^\circ)$ . (a) Temperature, (b) dimensionless radial stress, (c) dimensionless tangential stress, (d) dimensionless axial stress, (e) dimensionless shear stress, and (f) dimensionless von Mises stress.

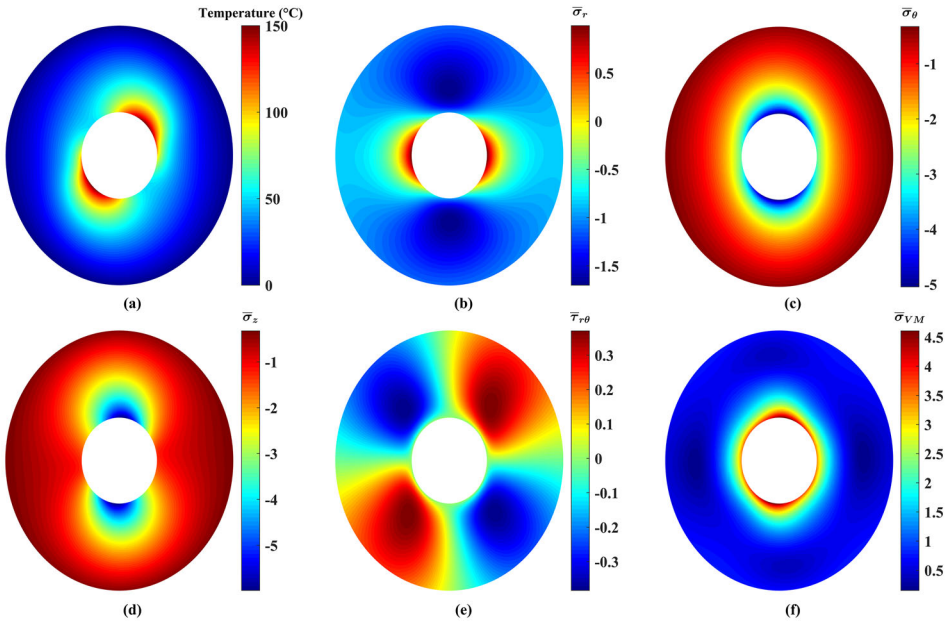


**Figure 12.** Resulting contours of the thermoelastic problem of 2D-FGC with  $f(\theta) = \cos(2\theta - 30^\circ)$ . (a) Temperature, (b) dimensionless radial stress, (c) dimensionless tangential stress, (d) dimensionless axial stress, (e) dimensionless shear stress, and (f) dimensionless von Mises stress.

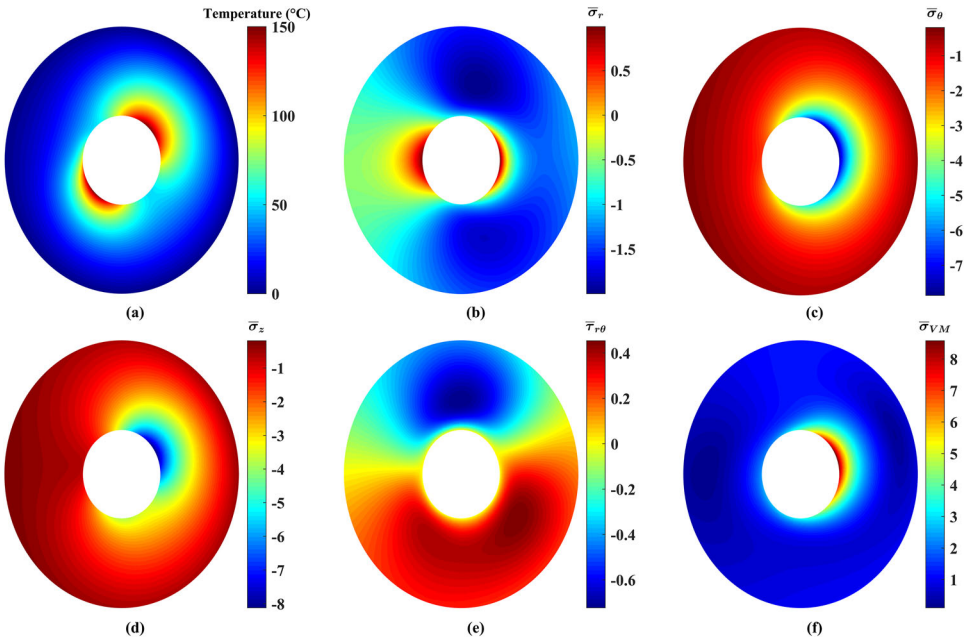


**Figure 13.** Resulting contours of the thermoelastic problem of 2D-FGC with  $f(\theta) = \cos(\theta + 130^\circ)$ . (a) Temperature, (b) dimensionless radial stress, (c) dimensionless tangential stress, (d) dimensionless axial stress, (e) dimensionless shear stress, and (f) dimensionless von Mises stress.

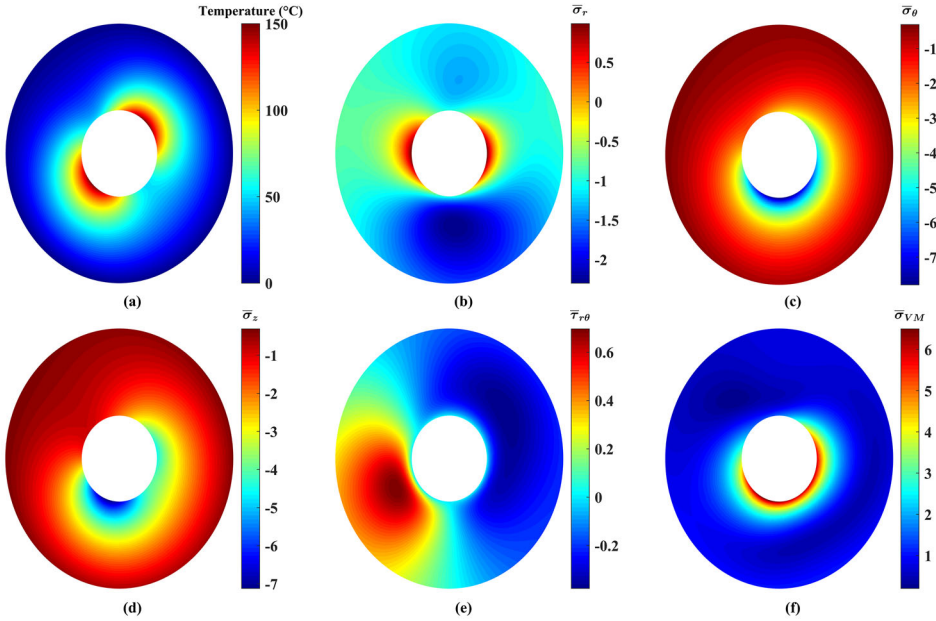


**Figure 14.** Resulting contours of the thermoelastic problem of 2D-FGC with  $f(\theta) = \cos(\theta - 120^\circ)$ . (a) Temperature, (b) dimensionless radial stress, (c) dimensionless tangential stress, (d) dimensionless axial stress, (e) dimensionless shear stress, and (f) dimensionless von Mises stress.

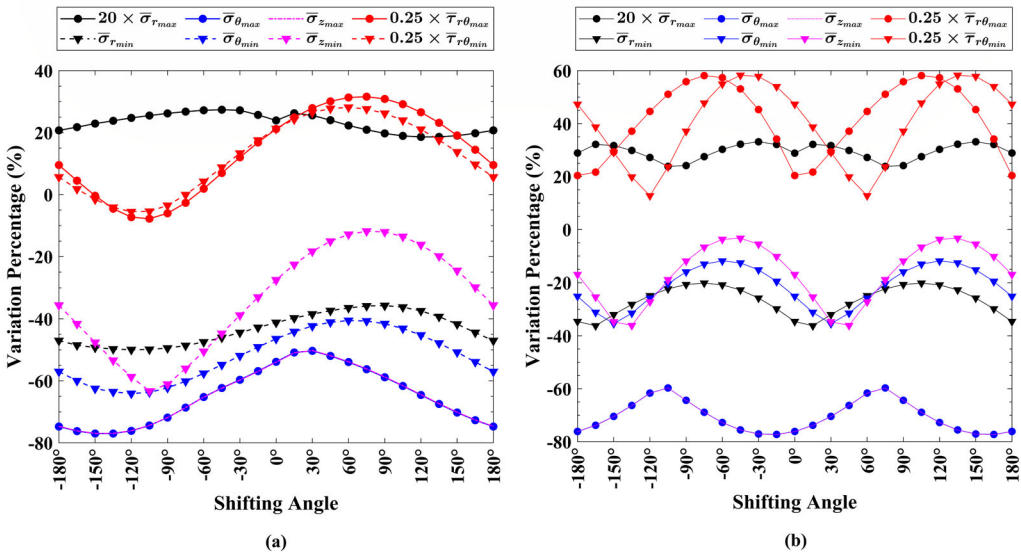


**Figure 15.** Variation's percentage for each stress component for the thermoelastic problem of 2D-FGC with  $f(\theta) = \cos(n_\theta \theta + s)$ . (a)  $n_\theta = 2$ , and (b)  $n_\theta = 1$ .

$$\sigma_{VM} = \frac{1}{\sqrt{2}} \left( (\sigma_r - \sigma_\theta)^2 + (\sigma_\theta - \sigma_z)^2 + (\sigma_z - \sigma_r)^2 + 6\tau_{r\theta}^2 \right)^{1/2} \quad (16)$$

Figure 10 shows that  $\bar{\sigma}_r$  varied between  $-3.06$  and  $1$ ,  $-0.81 \leq \bar{\sigma}_\theta \leq 10.5$ ,  $-9.8 \leq \bar{\sigma}_z \leq -0.8$ , and  $\bar{\sigma}_{VMmax}$  stood at approximately  $9.98$ . Also, the upper and lower limits of  $\bar{\tau}_{r\theta}$  leveled off at

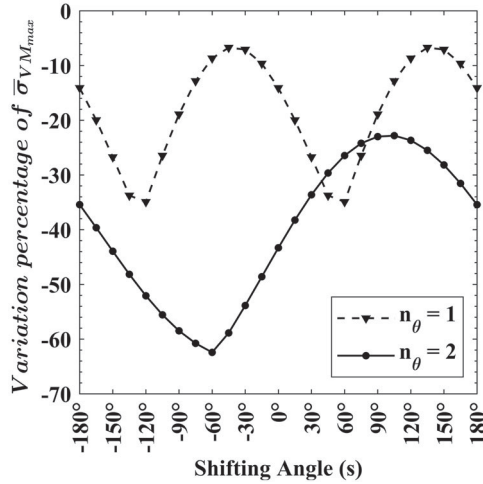


**Figure 16.** Maximum value of the dimensionless von Mises stress ( $\bar{\sigma}_{VM_{max}}$ ) reduction's percentage.

**Table 1.** The pertinent numerical values of some parameters used while investigating different values of  $n_\theta$  of 2D-FGC under thermomechanical loading conditions.

	Case (1)	Case (2)	Case (3)	Case (4)
$n_p$	2	1	2	2
$n_T$	2	2	1	1
$p_0$ (MPa)	100	100	100	2
$T_0$ ( $^{\circ}$ C)	100	100	100	1000

$\pm 0.25$ . Such results resemble a confirmation of the previous studies that  $\sigma_\theta$  has noteworthy influences on the cylinder's performance [14, 44].

For 2D-FGMs, only  $n_\theta = 2$  ( $s = +90^\circ$  and  $-30^\circ$ ) and  $n_\theta = 1$  ( $s = 180^\circ$  and  $-120^\circ$ ) are presented. The resulting temperature profiles are shown in Figures 11a–14a. It is seen that there are significant differences in their distributions as they are interconnected with  $k$ . Nevertheless, no impacts on the maximum and minimum  $T$  are seen since they are controlled by Eq. (15), and no heat generation is present in Eq. (7). But, it can be grasped that  $T$  in almost all regions tends to decrease except a small zone around the inner circumference. Consequently, profound effects are expected to encounter the stresses' readings that capitalize on  $T$ .

These induced stresses are plotted in Figures 11–14. It can be figured out that the usage of 2D-FGMs brought about drastic reductions in  $\bar{\sigma}_{r_{min}}$ ,  $\bar{\sigma}_\theta$ , and  $\bar{\sigma}_z$ . Until this juncture, 2D-FGMs are far better than 1D-FGMs. Two tiny drawbacks are noticed. First, the maximum tensile  $\bar{\sigma}_r$  tends to slightly grow. Second, at certain values of  $s$ ,  $\bar{\sigma}_{r\theta}$  shows small rise. Nevertheless, the declines in  $\bar{\sigma}_\theta$  and  $\bar{\sigma}_z$  substantially outweigh those increases, which have negligible impacts on  $\bar{\sigma}_{VM}$ .

In numbers, the values of  $\bar{\sigma}_{r_{max}}$  witnessed slight growths. Conversely,  $\bar{\sigma}_{r_{min}}$ , which is critical than  $\bar{\sigma}_{r_{max}}$ , dropped significantly. For instance, in Figure 11b, it reached  $-2.3$  at  $n_\theta = 2$  and  $s = 90^\circ$  that resembles about 75.2% of the value of the 1D-FGC. Likewise,  $\bar{\sigma}_{\theta_{max}}$  and  $\bar{\sigma}_{\theta_{min}}$  experienced substantial plunges. For example, at  $n_\theta = 2$  and  $s = -30^\circ$  (Figure 12c), they decreased by around 59% and 51%, respectively. Despite that,  $\bar{\sigma}_{\theta_{min}}$  is still the serious one since it has larger absolute value compared to  $\bar{\sigma}_{\theta_{max}}$ . Generally, for the selected values of  $n_\theta$  and  $s$ , the decline percentage for  $\bar{\sigma}_{\theta_{min}}$  is confined between the previous percentage (51%) and about half of it ( $\sim 25\%$ ) (Figure 13c:  $n_\theta = 1$  and  $s = 180^\circ$ ). Similar behaviors are noticed for  $\bar{\sigma}_z$ . In Figure 14d, for instance, the critical value of  $\bar{\sigma}_z$  went down by  $\sim 27\%$  if compared to the value at  $f(\theta) = 1$  shown in Figure 10d. This percentage rose reaching nearly 38% at  $n_\theta = 2$  and  $s = -30^\circ$  (Figure 12d).

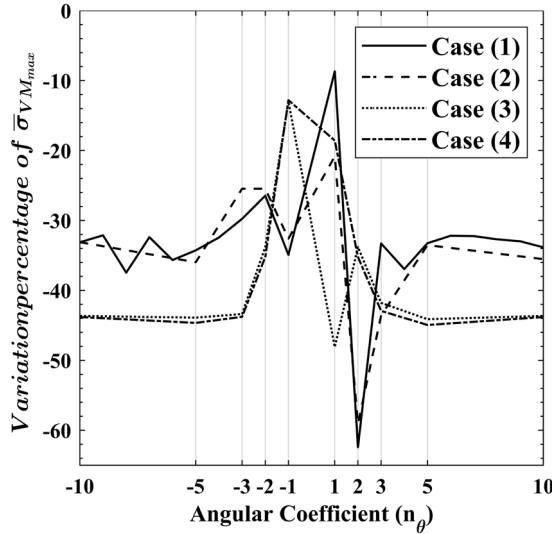


**Figure 17.** Variation of  $\bar{\sigma}_{VM_{max}}$  with  $n_\theta$  using different values of  $n_p$ ,  $n_T$ ,  $p_0$ , and  $T_0$ .

Such declines are considerably beneficial for raising the working loads and avoiding the occurrence of plasticity (failure) as appears in the reduction of  $\bar{\sigma}_{VM}$  (Figures 11f–14f). It is evident that there are variations in the values of  $\bar{\sigma}_{VM_{max}}$  based on  $s$  and  $n_\theta$ . Using  $s = 90^\circ$  with  $n_\theta = 2$ , yielded a decline in  $\bar{\sigma}_{VM_{max}}$  by  $\sim 22\%$  (Figure 11f). It grew to almost 54% if  $s$  is switched to  $-30^\circ$  (Figure 12f). Moreover, nearly two-thirds of that two values are applicable when  $n_\theta = 1$  prevails with  $s = 180^\circ$  (Figure 13f) and  $s = -120^\circ$  (Figure 14f), respectively.

Furthermore, Figure 15a,b presents the variations' percentages occurring in each stress component at different values of  $s$  at  $n_\theta = 2$  and  $n_\theta = 1$ , respectively. First, it is seen that the sign of  $s$  yields dissimilar results in contrast to the previous case (mechanical load only). Second, the change in  $\bar{\sigma}_{r_{max}}$  is negligible if compared to the change of  $\bar{\sigma}_{r_{min}}$ . Third, in Figure 15a, except at  $n_\theta = 2$  ( $s = -90^\circ, -120^\circ, -150^\circ$ ), the upper and lower values of  $\bar{\tau}_{r\theta}$  experienced gigantic rises. Despite that, these numbers are tricky since they are less than unity. For example, at  $n_\theta = 1$  and  $s = -30^\circ$  (Figure 15b),  $\bar{\tau}_{r\theta_{max}}$  increased slightly from  $\sim 0.25$  to  $\sim 0.7$ . Fourth, considering  $f(\theta)$  brought about considerable declines in  $\bar{\sigma}_{z_{min}}$  which is more important than  $\bar{\sigma}_{z_{max}}$  since  $|\bar{\sigma}_{z_{min}}| \gg |\bar{\sigma}_{z_{max}}|$ . Though the latter also witnessed massive drops, it can be neglected as they are fractions of one.

Finally, since  $\bar{\sigma}_{\theta_{min}}$  as well as  $\bar{\sigma}_{z_{min}}$  have the largest absolute values compared to other stress values, the change in  $\bar{\sigma}_{VM}$  is considerably influenced by their variation. In Figure 16, it can be deduced that  $\bar{\sigma}_{VM_{max}}$  declined with different ranges despite the often misleading growth of  $\bar{\tau}$  and parts of  $\bar{\sigma}_r$ . This decline hits almost 27% at  $n_\theta = 2$  and  $s = 60^\circ$ . At that instant as shown in Figure 15a,  $\bar{\tau}_{r\theta_{max}}$  grew by approximately 125% and  $\bar{\sigma}_{\theta_{min}}$  fell by  $\sim 40\%$ . Moreover, the use of  $s = -60^\circ$  produced the largest decrease for  $\bar{\sigma}_{VM_{max}}$  ( $\sim 63\%$ ) at  $n_\theta = 2$ . Nearly half of that value is the most applicable reduction percentage if  $n_\theta = 1$  is used. That shows that  $n_\theta = 2$  is more advantageous than  $n_\theta = 1$ .

However, until now, the analyses in the study are restricted to  $n_\theta = 1$  or 2. This forms the foundation of the next part, where different values of  $n_\theta$  are examined, i.e.,  $n_\theta = \pm 1, \pm 2, \pm 3, \pm 5$ , and  $\pm 10$ . Four cases are explored at  $s = -60^\circ$ . In this part, along with the variation of  $n_\theta$ , the values of  $n_p$ ,  $n_T$ ,  $p_0$ , and  $T_0$  are altered and listed in Table 1.

To avoid redundancy of results, only the variation of  $\bar{\sigma}_{VM_{max}}$  is presented in lieu of all the stress components. Figure 17 concludes that it is not always ensured to have  $n_\theta = 2$  to attain the greatest reduction in  $\bar{\sigma}_{VM_{max}}$ . In case (1),  $n_\theta = 2$  produced the larger reduction in  $\bar{\sigma}_{VM_{max}}$  ( $\sim 63\%$ ) compared to the other values. This matches the patterns of the loads, where  $n_p = n_\theta = 2$ . In the

second case, also,  $n_\theta = 2$  is preferable despite changing  $n_p$  to 1 and keeping  $n_T = 2$ . By moving to the third case, it is seen that  $n_\theta = 1$  is better and yielded 48% drop in  $\bar{\sigma}_{VM,max}$ . From these three cases, it can come to a mind that having  $n_\theta = n_T$  would produce improved  $\bar{\sigma}_{VM,max}$ . But, this is not constantly true, and this is proven in the fourth case, where  $n_p = 2n_T = 2$ . The favorable  $n_\theta$  is found to be at  $\pm 5$ . This stark disagreement in such case with the three previous cases initiates due to the difference in both  $p_0$  and  $T_0$ . Therefore, it can be understood that they with  $n_p$  and  $n_\theta$  have strategic roles in determining the ideal value of  $n_\theta$  to be used.

## 5. Conclusion

In this study, a FE scheme was developed to check the efficiency of using 2D-FGMs in alleviating the elastic/thermoelastic stresses of FGCs. The power-law model was used to describe materials' property variation radially, and it was modified to make properties dependent on both the radial and tangential directions concurrently.

Interpreting results showed the beneficial role of considering 2D-FGMs in reducing most of the stress components through the cylinder, which allows for raising the load limits safely. Eminent findings upon applying 2D-FGMs are listed below:

- The tangential stress has the upper hand in determining the behaviors of cylinders. In the second place comes the axial stress that arises in plane strain conditions.
- In case of mechanical loading: the radial, tangential, and shear stress components experienced declines in their values.
- In case of thermomechanical loading: the radial and shear stresses experienced variations in their readings. Conversely, other stresses decreased significantly. However, a decline in the von Mises stress was achieved with substantial values.
- Temperature in many regions of the cylinder tended to decline when the tangential variation of the thermal conductivity was considered, and this was the major cause for the variation of stresses.
- The sign of the shifting angle almost had no impact in the case of mechanical loading. In contrast, it had a great role when both thermal and mechanical loads were present together.
- The angular coefficient had significant impacts on the stresses' variation.

Eventually, different percentages of stresses' reductions are to be obtained if the gradation function is changed with its parameters (i.e., heterogeneity (grading) index). Therefore, it is recommended to optimize the angular coefficient and the shifting angle to obtain the global optimum of the stress components. This would be compulsory in case of complex loading and mixed boundary conditions. However, if 2D-FGMs are used without optimizing its associated parameters, inevitable drops of the stresses would occur.

## Data availability

The raw/processed data required to reproduce these findings cannot be shared at this time as the data also forms part of an ongoing study.

## Disclosure statement

The authors declared no potential conflicts of interest with respect to the research, authorship, and/or publication of this article.

## ORCID

A. M. Eldeeb  <http://orcid.org/0000-0002-3762-5683>  
 Y. M. Shabana  <http://orcid.org/0000-0001-7225-1579>  
 T. A. El-Sayed  <http://orcid.org/0000-0002-1494-5334>  
 Licheng Guo  <http://orcid.org/0000-0002-7834-1978>  
 A. Elsawaf  <http://orcid.org/0000-0002-9971-2088>

## References

- [1] P. H. Cong, *et al.*, “Nonlinear thermomechanical buckling and post-buckling response of porous FGM plates using Reddy’s HSDT,” *Aerosp. Sci. Technol.*, vol. 77, pp. 419–428, 2018. DOI: [10.1016/j.ast.2018.03.020](https://doi.org/10.1016/j.ast.2018.03.020).
- [2] D. Kouider, *et al.*, “An original four-variable quasi-3D shear deformation theory for the static and free vibration analysis of new type of sandwich plates with both FG face sheets and FGM hard core,” *Steel Compos. Struct.*, vol. 41, no. 2, pp. 167–191, 2021. DOI: [10.12989/scs.2021.41.2.167](https://doi.org/10.12989/scs.2021.41.2.167).
- [3] L. Guo, *et al.*, “The interface crack problem for a functionally graded coating-substrate structure with general coating properties,” *Int. J. Solids Struct.*, vol. 146, pp. 136–153, 2018. DOI: [10.1016/j.ijsolstr.2018.03.025](https://doi.org/10.1016/j.ijsolstr.2018.03.025).
- [4] S. Huang, *et al.*, “The interface crack problem under steady heat flux for a functionally graded coating-substrate structure with general coating properties,” *Theor. Appl. Fract. Mech.*, vol. 109, pp. 102675, 2020. DOI: [10.1016/j.tafmec.2020.102675](https://doi.org/10.1016/j.tafmec.2020.102675).
- [5] M. Jabbari, M. Meshkini, and M. R. Eslami, “Mechanical and thermal stresses in FGPPM hollow cylinder due to radially symmetric loads,” *J. Pressure Vessel Technol.*, vol. 138, no. 1, pp. 2938–2946, 2016. DOI: [10.1115/1.4031372](https://doi.org/10.1115/1.4031372).
- [6] M. Jabbari, M. Meshkini, and M. R. Eslami, “Nonaxisymmetric mechanical and thermal stresses in FGPPM hollow cylinder,” *J. Pressure Vessel Technol.*, vol. 134, no. 6, pp. 1–25, 2012. DOI: [10.1115/1.4007034](https://doi.org/10.1115/1.4007034).
- [7] J. Jafari Fesharaki, *et al.*, “Two-dimensional solution for electro-mechanical behavior of functionally graded piezoelectric hollow cylinder,” *Appl. Math. Model.*, vol. 36, no. 11, pp. 5521–5533, 2012. DOI: [10.1016/j.apm.2012.01.019](https://doi.org/10.1016/j.apm.2012.01.019).
- [8] Y. V. Tokovyy and C.-C. Ma, “Analytical solutions to the planar non-axisymmetric elasticity and thermoelasticity problems for homogeneous and inhomogeneous annular domains,” *Int. J. Eng. Sci.*, vol. 47, no. 3, pp. 413–437, 2009. DOI: [10.1016/j.ijengsci.2008.10.005](https://doi.org/10.1016/j.ijengsci.2008.10.005).
- [9] R. C. Batra and G. J. Nie, “Analytical solutions for functionally graded incompressible eccentric and non-axisymmetrically loaded circular cylinders,” *Compos. Struct.*, vol. 92, no. 5, pp. 1229–1245, 2010. DOI: [10.1016/j.compstruct.2009.10.022](https://doi.org/10.1016/j.compstruct.2009.10.022).
- [10] A. Loghman, M. Nasr, and M. Arefi, “Nonsymmetric thermomechanical analysis of a functionally graded cylinder subjected to mechanical, thermal, and magnetic loads,” *J. Therm. Stresses*, vol. 40, no. 6, pp. 765–782, 2017. DOI: [10.1080/01495739.2017.1280380](https://doi.org/10.1080/01495739.2017.1280380).
- [11] A. M. Eldeeb, Y. M. Shabana, and A. Elsawaf, “Investigation of the thermoelastoplastic behaviors of multi-layer FGM cylinders,” *Compos. Struct.*, vol. 276, pp. 114523, 2021. DOI: [10.1016/j.compstruct.2021.114523](https://doi.org/10.1016/j.compstruct.2021.114523).
- [12] M. Hosseini, M. Shishesaz, and A. Hadi, “Thermoelastic analysis of rotating functionally graded micro/nano-disks of variable thickness,” *Thin-Walled Struct.*, vol. 134, pp. 508–523, 2019. DOI: [10.1016/j.tws.2018.10.030](https://doi.org/10.1016/j.tws.2018.10.030).
- [13] P. Nayak, S. Bhowmick, and K. N. Saha, “Elasto-plastic analysis of thermo-mechanically loaded functionally graded disks by an iterative variational method,” *Eng. Sci. Technol. Int. J.*, vol. 23, no. 1, pp. 42–64, 2020. DOI: [10.1016/j.jestch.2019.04.007](https://doi.org/10.1016/j.jestch.2019.04.007).
- [14] A. M. Eldeeb, Y. M. Shabana, and A. Elsawaf, “Influences of angular deceleration on the thermoelastoplastic behaviors of nonuniform thickness multilayer FGM discs,” *Compos. Struct.*, vol. 258, pp. 113092, 2021. DOI: [10.1016/j.compstruct.2020.113092](https://doi.org/10.1016/j.compstruct.2020.113092).
- [15] A. M. Eldeeb, Y. M. Shabana, and A. Elsawaf, “Thermo-elastoplastic behavior of a rotating sandwich disc made of temperature-dependent functionally graded materials,” *J. Sandwich Struct. Mater.*, vol. 23, no. 5, pp. 1761–1783, 2021. DOI: [10.1177/1099636220904970](https://doi.org/10.1177/1099636220904970).
- [16] Y. M. Shabana and A. Elsawaf, “Nonlinear multi-variable optimization of layered composites with nontraditional interfaces,” *Struct. Multidisc. Optim.*, vol. 52, no. 5, pp. 991–1000, 2015. DOI: [10.1007/s00158-015-1292-2](https://doi.org/10.1007/s00158-015-1292-2).
- [17] Y. M. Shabana, *et al.*, “Stresses minimization in functionally graded cylinders using particle swarm optimization technique,” *Int. J. Pressure Vessels Piping*, vol. 154, pp. 1–10, 2017. DOI: [10.1016/j.ijpvp.2017.05.013](https://doi.org/10.1016/j.ijpvp.2017.05.013).
- [18] A. M. Eldeeb, Y. M. Shabana, and A. Elsawaf, “Particle swarm optimization for the thermoelastic behaviors of functionally graded rotating nonuniform thickness sandwich discs,” *Arab. J. Sci. Eng.*, pp. 1–13, 2022. DOI: [10.1007/s13369-022-07351-x](https://doi.org/10.1007/s13369-022-07351-x).
- [19] S. Zhou and Q. Li, “Microstructural design of connective base cells for functionally graded materials,” *Mater. Lett.*, vol. 62, no. 24, pp. 4022–4024, 2008. DOI: [10.1016/j.matlet.2008.05.058](https://doi.org/10.1016/j.matlet.2008.05.058).



- [20] Y. Su, *et al.*, “Influence of composition gradient variation on the microstructure and mechanical properties of 316L/Inconel718 functionally graded material fabricated by laser additive manufacturing,” *J. Mater. Process. Technol.*, vol. 283, pp. 116702, 2020. DOI: [10.1016/j.jmatprotec.2020.116702](https://doi.org/10.1016/j.jmatprotec.2020.116702).
- [21] Nemat-Alla, M. K. I. E. Ahmed, and I. Hassab-Allah, “Elastic–plastic analysis of two-dimensional functionally graded materials under thermal loading,” *Int. J. Solids Struct.*, vol. 46, no. 14–15, pp. 2774–2786, 2009. DOI: [10.1016/j.ijsolstr.2009.03.008](https://doi.org/10.1016/j.ijsolstr.2009.03.008).
- [22] X.-Y. Miao, *et al.*, “Free vibration analysis of three-layer thin cylindrical shell with variable thickness two-dimensional FGM middle layer under arbitrary boundary conditions,” *J. Sandwich Struct. Mater.*, vol. 24, no. 2, pp. 973–1003, 2022. DOI: [10.1177/109963622111020429](https://doi.org/10.1177/109963622111020429).
- [23] M. Nemat-Alla, “Reduction of thermal stresses by developing two-dimensional functionally graded materials,” *Int. J. Solids Struct.*, vol. 40, no. 26, pp. 7339–7356, 2003. DOI: [10.1016/j.ijsolstr.2003.08.017](https://doi.org/10.1016/j.ijsolstr.2003.08.017).
- [24] N. T. Hong, “Nonlinear static bending and free vibration analysis of bidirectional functionally graded material plates,” *Int. J. Aerosp. Eng.*, vol. 2020, pp. 1–16, 2020. DOI: [10.1155/2020/8831366](https://doi.org/10.1155/2020/8831366).
- [25] M. Nemat-Alla, “Reduction of thermal stresses by composition optimization of two-dimensional functionally graded materials,” *Acta Mech.*, vol. 208, no. 3–4, pp. 147–161, 2009. DOI: [10.1007/s00707-008-0136-1](https://doi.org/10.1007/s00707-008-0136-1).
- [26] A. Najibi and M. H. Shojaeefard, “Elastic mechanical stress analysis in a 2D-FGM thick finite length hollow cylinder with newly developed material model,” *Acta Mech. Solida Sin.*, vol. 29, no. 2, pp. 178–191, 2016. DOI: [10.1016/S0894-9166\(16\)30106-9](https://doi.org/10.1016/S0894-9166(16)30106-9).
- [27] A. Najibi, “Mechanical stress reduction in a pressurized 2D-FGM thick hollow cylinder with finite length,” *Int. J. Pressure Vessels Piping*, vol. 153, pp. 32–44, 2017. DOI: [10.1016/j.ijpvp.2017.05.007](https://doi.org/10.1016/j.ijpvp.2017.05.007).
- [28] A. Najibi and R. Talebitooti, “Nonlinear transient thermo-elastic analysis of a 2D-FGM thick hollow finite length cylinder,” *Compos. Part B: Eng.*, vol. 111, pp. 211–227, 2017. DOI: [10.1016/j.compositesb.2016.11.055](https://doi.org/10.1016/j.compositesb.2016.11.055).
- [29] Moussavinezhad, S. M. F. Shahabian, S. and M. Hosseini, “Two-dimensional stress-wave propagation in finite-length FG cylinders with two-directional nonlinear grading patterns using the MLPG method,” *J. Eng. Mech.*, vol. 140, no. 3, pp. 575–592, 2014. DOI: [10.1061/\(ASCE\)EM.1943-7889.0000678](https://doi.org/10.1061/(ASCE)EM.1943-7889.0000678).
- [30] A. Salehi and I. Ahmadi, “Transient thermal and mechanical stress analysis of 2D-functionally graded finite cylinder: A truly meshless formulation,” *Iran J. Sci. Technol. Trans. Mech. Eng.*, vol. 46, no. 3, pp. 573–598, 2022. DOI: [10.1007/s40997-021-00432-6](https://doi.org/10.1007/s40997-021-00432-6).
- [31] M. Meshkini, *et al.*, “Asymmetric mechanical and thermal stresses in 2D-FGPPMs hollow cylinder,” *J. Therm. Stresses*, vol. 40, no. 4, pp. 448–469, 2017. DOI: [10.1080/01495739.2016.1249987](https://doi.org/10.1080/01495739.2016.1249987).
- [32] A. Najibi and G. Jing, “Two dimensional stress wave propagation analysis of infinite 2D-FGM hollow cylinder,” *Waves Random Complex Media*, pp. 1–18, 2021. DOI: [10.1080/17455030.2021.1987584](https://doi.org/10.1080/17455030.2021.1987584).
- [33] M. Saadatfar and M. H. Zarandi, “Effect of angular acceleration on the mechanical behavior of an exponentially graded piezoelectric rotating annular plate with variable thickness,” *Mech. Based Des. Struct. Mach.*, vol. 50, no. 4, pp. 1354–1370, 2022. DOI: [10.1080/15397734.2020.1751198](https://doi.org/10.1080/15397734.2020.1751198).
- [34] V. Vullo and F. Vivio, *Rotors: Stress Analysis and Design*. New York: Springer Science & Business Media, 2013.
- [35] J. N. Reddy and D. K. Gartling, *The Finite Element Method in Heat Transfer and Fluid Dynamics*. Boca Raton: CRC press, 2010.
- [36] A. J. M. Ferreira and N. Fantuzzi, *Plane Stress, in MATLAB Codes for Finite Element Analysis: Solids and Structures*. Cham: Springer International Publishing, 2020, pp. 171–205.
- [37] H. Li and Y. Liu, “Functionally graded hollow cylinders with arbitrary varying material properties under non-axisymmetric loads,” *Mech. Res. Commun.*, vol. 55, pp. 1–9, 2014. DOI: [10.1016/j.mechrescom.2013.10.011](https://doi.org/10.1016/j.mechrescom.2013.10.011).
- [38] S. H. Kordkheili and R. Naghdabadi, “Thermoelastic analysis of a functionally graded rotating disk,” *Compos. Struct.*, vol. 79, no. 4, pp. 508–516, 2007. DOI: [10.1016/j.compstruct.2006.02.010](https://doi.org/10.1016/j.compstruct.2006.02.010).
- [39] N. Tutuncu and B. Temel, “A novel approach to stress analysis of pressurized FGM cylinders, disks and spheres,” *Compos. Struct.*, vol. 91, no. 3, pp. 385–390, 2009. DOI: [10.1016/j.compstruct.2009.06.009](https://doi.org/10.1016/j.compstruct.2009.06.009).
- [40] A. Hassani, *et al.*, “Semi-exact elastic solutions for thermo-mechanical analysis of functionally graded rotating disks,” *Compos. Struct.*, vol. 93, no. 12, pp. 3239–3251, 2011. DOI: [10.1016/j.compstruct.2011.06.001](https://doi.org/10.1016/j.compstruct.2011.06.001).
- [41] A. Hassani, *et al.*, “Semi-exact solution for thermo-mechanical analysis of functionally graded elastic-strain hardening rotating disks,” *Commun. Nonlinear Sci. Numeric. Simul.*, vol. 17, no. 9, pp. 3747–3762, 2012. DOI: [10.1016/j.cnsns.2012.01.026](https://doi.org/10.1016/j.cnsns.2012.01.026).
- [42] M. Bayat, *et al.*, “Mechanical and thermal stresses in a functionally graded rotating disk with variable thickness due to radially symmetry loads,” *Int. J. Pressure Vessels Piping*, vol. 86, no. 6, pp. 357–372, 2009. DOI: [10.1016/j.ijpvp.2008.12.006](https://doi.org/10.1016/j.ijpvp.2008.12.006).
- [43] R. M. Jones, *Deformation Theory of Plasticity*. Blacksburg: Bull Ridge Corporation, 2009.
- [44] F. Vivio, V. Vullo and P. Cifani, “Theoretical Stress Analysis of Rotating Hyperbolic Disk without Singularities Subjected to Thermal Load,” *J. Thermal Stresses*, vol. 37, no. 2, pp. 117–136, 2014. DOI: [10.1080/01495739.2013.839526](https://doi.org/10.1080/01495739.2013.839526).